Inorganic Chemistry

Article

pubs.acs.org/IC

Series of Metal Organic Frameworks Assembled from Ln(III), Na(I), and Chiral Flexible-Achiral Rigid Dicarboxylates Exhibiting Tunable UV−vis−IR Light Emission

Zakariae Amghouz,* Santiago García-Granda, and José R. García

Departamentos de Química Física y Analítica y Química Orgánica e Inorgánica, Universidad de Oviedo, 33006 Oviedo-CINN, Spain

Rute A. S. Ferreira, Luís Mafra, Luis D. Carlos, and João Rocha

Departments of Chemistry & Physics, CICECO, University of Aveiro, 3810-193 Aveiro, Portugal

Supporting Information

ABSTRACT: Two series of isoreticular chiral metal−organic frameworks assembled from Ln(III) (Ln = Sm, Eu, Gd, Tb, Dy, Ho, Er, Yb), Na(I), and chiral flexible-achiral rigid dicarboxylate ligands, formulated as [NaLn(Tart)(BDC)-$(H_2O)_2$] (**S1**) and [NaLn(Tart)(biBDC)$(H_2O)_2$] (**S2**) (H_2Tart = tartaric acid; H_2BDC = terephthalic acid; H_2biBDC = biphenyl-4,4′-dicarboxylic acid), were obtained as single phases under hydrothermal conditions. The compounds have been studied by single-crystal and powder X-ray diffraction, thermal analyses (TG-MS and DSC), vibrational spectroscopy (FTIR), scanning electron microscopy (SEM-EDX), elemental analysis, and X-ray thermodiffractometry. The catalytic activity has been also investigated. The photoluminescence properties of selected compounds have been investigated, exhibiting room temperature tunable UV−vis−IR light emission.

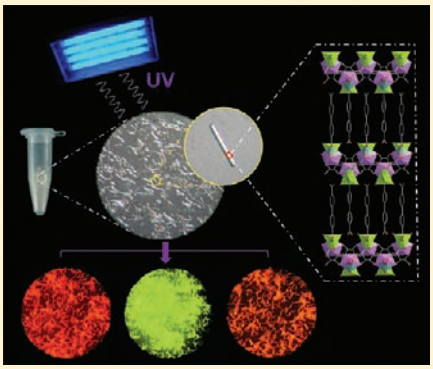

INTRODUCTION

Lanthanide ions attract a great deal of interest because their luminescence properties are useful in a variety of photonic applications; the most prominent are optical amplification for telecommunication,[1] light emitting diodes,[2] lasers or tunable lasers,[3] low-energy scintillators,[4] and fluoro-immuno assays.[5] The luminescence of the lanthanide ions stems from intra 4f-transitions, which are in principle forbidden transitions resulting in relatively long-lived excited states, and hence makes them suited for laser applications. The luminescence of lanthanide(III) ions, such as europium and terbium, emitting in the visible range, are useful for fluorescent lighting and color displays.[6] Those emitting in the near-infrared region are ideally suited for biological imaging and telecommunication applications.[7] Er(III) is acually used as the active component in optical amplification in erbium doped fiber amplifiers (EDFAs)[1] in telecommunication devices. Ultraviolet light-emitting devices (UVLEDs) are strong candidates in lighting equipment and optical storage devices.[8] Therefore, luminescent materials which can give tunable emissions between UV−vis−infrared wavelengths are attractive targets for both fundamental research and practical applications.

A particular class of materials known as metal−organic frameworks (or coordination polymers) based on trivalent lanthanides (LnMOFs), composed of metal ions or metal clusters as nodes and multifunctional organic linkers as molecular building blocks through strong bonds, are a very promising class of materials and may constitute a robust platform for addressing the challenges in engineering of luminescent centers for multipurposes. MOFs have emerged as a new class of materials, basically due to their potential applications in gas storage[9−17] and separation.[18−21]

Studies on the photoluminescence of MOFs are still in their infancy,[22,23] and are missing for an integrated approach toward the design of efficient, stable, cheap, environmentally friendly, and multiluminescent LnMOFs.[23] The research on luminescent LnMOFs has been focused on their visible emission features. As noted in the majority of reported LnMOFs, the studies of luminescence properties are limited to structures containing Eu(III) and/or Tb(III),[24−40] owing to their efficient and spectrally narrow red and green emissions and their energy level scheme that allows their use as a sensitive local probe of the metal neighborhood, in addition to their sensitization via ligand levels (the well-known antenna effect), which makes their compounds an attractive target. However, emissive near-infrared (NIR) LnMOFs have been barely investigated mainly because in organic matrices molecular vibrations like C−H and O−H stretching modes quench the lanthanide excited states. Nevertheless, it is possible to overcome such limitations through rational structural design. A few instances so far of NIR emitting

Received: September 15, 2011
Published: December 29, 2011

   dx.doi.org/10.1021/ic202020z | *Inorg. Chem.* 2012, 51, 1703−1716

LnMOFs from less common lanthanides, such as Er(III), Nd(III), and Yb(III), have been reported.[41−48]

Recently, the amount of efforts devoted to the field of photoluminescence of MOFs is increasing, and some novel interesting phenomena have been discovered, such as tunable UV-to-visible emission by controlling the guest molecules,[49] tunable yellow-to-white emission or white-to-purplish blue by variation of excitation wavelength,[50] tunable color by changing the doping concentration,[25,] tunable visible-IR changing the doping element,[51] tunable emissions by controlling the type of guest species,[52] and ion and small molecules sensing.[53,54] However, to the best of our knowledge, no tunable UV−vis−NIR luminescent chiral LnMOFs have been reported so far.

Herein, we report the synthesis and structural characterization of two new families (**S1** and **S2**), which consists of 16 isoreticular trivalent lanthanide-organic frameworks containing Ln(III), Na(I), and both flexible and rigid dicarboxylate ligands, motivated by our previous report,[55] as a tunable platform for the design of stable, cheap, and efficient multiwavelength emission materials with intriguing architectures.

EXPERIMENTAL SECTION

Synthesis. $LnNa(C_4H_4O_6)(C_8H_4O_4)(H_2O)_2$ (Series 1) and $LnNa(C_4H_4O_6)(C_{14}H_8O_4)(H_2O)_2$ (Series 2) were synthesized under hydrothermal conditions and obtained as a single phase of colorless needle crystals by following similar procedures.

*Series 1 (**S1**).* In a typical synthesis, 0.21 g (1.4 mmol) of L-tartaric acid (H_2Tart), 0.08 g (0.5 mmol) of terephthalic acid (H_2BDC), 0.14 g (3.5 mmol) of NaOH, and $LnCl_3{\cdot}6H_2O$ (Sm: 0.30 g, 0.82 mmol; Eu: 0.28 g, 0.76 mmol; Gd: 0.29 g, 0.77 mmol; Tb: 0.30 g, 0.80 mmol; Dy: 0.30 g 0.80 mmol; Ho: 0.33 g, 0.88 mmol; Er: 0.36 g, 0.94 mmol; Yb: 0.40 g, 1 mmol) were dissolved in a mixture of ethanol (6 mL) and distilled water (6 mL).

*Series 2 (**S2**).* In a typical synthesis, 0.21 g (1.4 mmol) of L-tartaric acid (H_2Tart), 0.12 g (0.5 mmol) of biphenyl-4,4′-dicarboxylic acid (H_2biBDC), 0.14 g (3.5 mmol) of NaOH, and $LnCl_3{\cdot}6H_2O$ (Sm: 0.30 g, 0.82 mmol; Eu: 0.27 g, 0.74 mmol; Gd: 0.28 g, 0.75 mmol; Tb: 0.33 g, 0.88 mmol; Dy: 0.31 g 0.82 mmol; Ho: 0.34 g, 0.90 mmol; Er: 0.37 g, 0.97 mmol; Yb: 0.39 g, 1 mmol) were dissolved in a mixture of ethanol (6 mL) and distilled water (6 mL).

In both cases, the reaction mixture was stirred for 2 h at room temperature to homogeneity and then placed in a Teflon-lined stainless vessel (40 mL) and heated to 170 °C for 60 h under autogenous pressure and afterward cooled slowly to room temperature at a rate of 5 °C/h. The resulting product was filtered off, washed thoroughly with ethanol and distilled water, and finally air-dried in an oven at 60 °C. Elemental analyses were performed in a C−H−N Perkin-Elmer model 2400B elemental analyzer. The yields based on lanthanides elements, the calculated and found percentages of C−H, and the total mass losses of the two series of compounds are represented in Table S1 (see Supporting Information).

Doped Yttrium Compounds. Compounds based on Ce, Pr, and Nd, unfortunately have not been obtained; thus, we have resorted to the doping approach of yttrium-based compounds by the following procedure: 0.21 g (1.4 mmol) of L-tartaric acid (H_2Tart), 0.08 g (0.5 mmol) of terephthalic acid (H_2BDC), and 0.14 g (3.5 mmol) of NaOH were added to 6 mL of a solution of Y:Ln with a ratio of 20:1 previously prepared by dissolving 0.29 g (0.95 mmol) of $YCl_3{\cdot}6H_2O$ and $LnCl_3{\cdot}6H_2O$ (for Ce: 0.019 g, 0.05 mmol; Pr: 0.013 g, 0.08 mmol; Nd: 0.018 g, 0.05 mmol) in 6 mL and stirring for 24 h. Finally, 6 mL of ethanol were added to the mixture. The reaction mixture was stirred for 1 h and then placed in a Teflon-lined stainless vessel (40 mL) and heated to 180 °C for 72 h (for Ce: 0.08 g, ca. 20% yield based on Y; Pr: 0.10 g, ca. 28%; Nd: 0.12 g, ca. 30%).

Single-Crystal X-ray Diffraction Studies. Data collection was performed at 293 K on an Agilent Gemini CCD diffractometer, using CuKα radiation. Images were collected at a 55 mm fixed crystal−detector distance, using the oscillation method, with 1° oscillation and variable exposure time per image. The crystal structure was solved by direct methods. The refinement was performed using full-matrix least-squares on F^2. All non-H atoms were anisotropically refined. All H atoms were either geometrically placed riding on their parent atoms or located from the difference Fourier map, with isotropic displacement parameters set to 1.2 times the U_{eq} of the atoms to which they are attached. Crystallographic calculations were carried out using the following programs: CrysAlis CCD[56] for data collection; CrysAlis RED[57] for cell refinement, data reduction and empirical absorption correction; SHELXS-97[58] or SIR-2004[59] for structure solution; XABS2[60] for refined absorption correction; SHELXL-97[58] for structure refinement and prepare materials for publication; PLATON[61] for the geometrical calculations; and Diamond[62] for molecular graphics. The detailed crystallographic data and the structure refinement parameters are summarized in Table 1. Selected bond distances, angles, and hydrogen bonds for **S1** and **S2** are given in Tables S2 and S3 (see Supporting Information).

Thermal Characterization. A Mettler-Toledo TGA/SDTA851^e and a DSC822e were used for the thermal analyses in oxygen dynamic atmosphere (50 mL/min) at a heating rate of 10 °C/min. In all cases, ca. 20 mg of powder sample was thermally treated, and blank runs were performed. In TG tests, a Pfeiffer Vacuum ThermoStar GSD301T mass spectrometer was used to determine the evacuated vapors. The masses 18 (H_2O), 44 (CO_2), and of the intense peaks corresponding to the cracking of the ligands BDC^{2-} and $biBDC^{2-}$, were tested by using a detector C-SEM, operating at 1200 V, with a time constant of 1 s.

Morphological Characterization. Micrographs and X-ray microanalysis (SEM/EDX) were recorded with a JEOL JSM-6100 electron microscope operating at 20 kV coupled with an INCA Energy-200 energy dispersive X-ray microanalysis system (EDX). SEM images show needle shaped crystals with length of ca. 50−400 μm (Supporting Information, Figure S1), and EDX confirmed that the Ln/Na ratio is ca. 1:1.

Infrared Spectra. The infrared data were collected at RT using a FT-IR Bruker Tensor-27 spectrometer from KBr pellets. The spectra were collected over the range 4000−400 cm^{-1} by averaging 15 scans at a maximum resolution of 4 cm^{-1}.

Powder X-ray Diffraction Studies. Powder X-ray diffraction patterns were recorded on Xpert Philips diffratometer with CuKα radiation. The samples were gently ground in an agate mortar in order to minimize the preferred orientation. All data were collected at room temperature over the angular 2θ range 3−46° with a step of 0.01° and a counting time of 1.5 s/step. The PXRD patterns of the compounds **1** and **2** were compared with the theoretical ones (Supporting Information, Figure S2), indicating that the products have been successfully obtained as pure crystalline phases.

Powder X-ray Thermodiffraction Studies. In two different diffractometers, the powder X-ray thermodiffraction studies were performed in (a) air, the sample was placed in an Anton Paar HTK 1200N oven-chamber, on a PANalytical XPERT-PRO diffractometer, using CuKα radiation, equipped with PIXcel linear detector with 255 channels. Each powder pattern was recorded in the 4−110° range (2θ) at intervals of 25 °C up to 200 °C and cooling down to 25 °C with a step of 0.013° and a counting time of 0.424 s/channel. The temperature ramp between two consecutive temperatures was 10 °C/min; (b) air, the sample was placed in an Anton Paar XRK 900 reactor chamber on a Bruker D8 Advance diffractometer with *DAVINCI* design, using CuKα radiation, equipped with LynxEye detector. Each powder pattern was recorded in the 4−60° range (2θ) from RT to 200 °C and cooling to RT with a step of 0.02° and a counting time of 0.4 s. The temperature ramp between two consecutive temperatures was 10 °C/min; (c) vacuum, the sample was placed in an Anton Paar XRK 900 reactor chamber on a Bruker D8 Advance diffractometer with *DAVINCI* design, using CuKα radiation, equipped with LynxEye detector. Each powder pattern was recorded in the 4−60° range (2θ) from RT to 900 °C with a step of 0.02° and a counting time of 0.3 s; the temperature ramp was 10 °C/min and XRPD patterns were recorded every 50 °C.

dx.doi.org/10.1021/ic202020z | *Inorg. Chem.* 2012, 51, 1703−1716

Table 1. Crystallographic Data for Series of Compounds S1 and S2

compound	3	4	5	6	7	8	9	10
identification code	Za3	Za5	Za7	Za9	Za11	Za13	Za15	Za17
empirical formula	C12 H12 Sm Na O12	C12 H12 Eu Na O12	C12 H12 Gd Na O12	C12 H12 Tb Na O12	C12 H12 Dy Na O12	C12 H12 Ho Na O12	C12 H12 Er Na O12	C12 H12 Yb Na O12
formula weight/g mol^{-1}	521.57	523.17	528.46	530.14	533.71	536.14	538.47	544.25
temperature/K	293(2)	293(2)	293(2)	293(2)	293(2)	293(2)	293(2)	293(2)
wavelength/Å	1.54184	1.54184	1.54184	1.54184	1.54184	1.54184	1.54184	1.54184
crystal system	orthorhombic	orthorhombic	orthorhombic	orthorhombic	orthorhombic	orthorhombic	orthorhombic	orthorhombic
space group	$C222_1$	$C222_1$	$C222_1$	$C222_1$	$C222_1$	$C222_1$	$C222_1$	$C222_1$
unit cell dimensions								
a (Å)	6.94220(10)	6.9287(3)	6.920(2)	6.9031(3)	6.89600(10)	6.8860(3)	6.8781(7)	6.8598(2)
b (Å)	30.5658(5)	30.460(2)	30.559(7)	30.4533(11)	30.4341(8)	30.3878(12)	30.389(3)	30.3257(8)
c (Å)	7.58420(10)	7.5611(4)	7.5478(14)	7.5215(2)	7.4984(2)	7.4722(4)	7.4593(6)	7.4274(2)
cell volume/ $Å^3$	1609.32(4)	1595.7(1)	1596.1(7)	1581.2(1)	1573.7(1)	1563.6(1)	1559.1(3)	1545.1(1)
Z	4	4	4	4	4	4	4	4
calc density/mg m^{-3}	2.153	2.178	2.199	2.227	2.253	2.278	2.294	2.34
absorption coefficient/mm^{-1}	28.30	28.98	27.79	22.91	26.33	10.38	10.92	12.13
$F(000)$	1012	1016	1020	1024	1028	1032	1036	1044
crystal size (mm^3)	0.01 × 0.02 × 0.11	0.01 × 0.01 × 0.17	0.01 × 0.04 × 0.13	0.01 × 0.03 × 0.32	0.01 × 0.02 × 0.11	0.01 × 0.01 × 0.11	0.01 × 0.03 × 0.11	0.02 × 0.03 × 0.14
theta range for data collection/°	5.79−70.52	2.89−71.94	5.79−71.49	5.81−70.56	5.82−68.25	5.82−70.61	2.91−70.69	5.84−68.17
index ranges	$-7 \le h \le 8$	$-8 \le h \le 8$	$-8 \le h \le 8$	$-7 \le h \le 8$	$-8 \le h \le 8$	$-8 \le h \le 6$	$-8 \le h \le 6$	$-7 \le h \le 8$
	$-33 \le k \le 36$	$-37 \le k \le 21$	$-37 \le k \le 36$	$-36 \le k \le 35$	$-34 \le k \le 36$	$-36 \le k \le 36$	$-36 \le k \le 36$	$-35 \le k \le 36$
	$-9 \le l \le 8$	$-6 \le l \le 9$	$-9 \le l \le 8$	$-9 \le l \le 5$	$-7 \le l \le 8$	$-8 \le l \le 8$	$-8 \le l \le 9$	$-8 \le l \le 4$
reflections collected	3417	2939	14896	3163	4447	3015	7667	2809
independent reflections	1537 [R(int) = 0.04]	1556 [R(int) = 0.05]	1554 [R(int) = 0.06]	1498 [R(int) = 0.04]	1429 [R(int) = 0.06]	1460 [R(int) = 0.05]	1508 [R(int) = 0.06]	1405 [R(int) = 0.03]
completeness to $theta_{max}$ (%)	99.70	99.50	99.80	99.50	99.20	99.60	99.80	99.70
absorption correction	refined (XABS2)	refined (XABS2)	refined (XABS2)	refined (XABS2)	refined (XABS2)	refined (XABS2)	refined (XABS2)	refined (XABS2)
max and min transmission	0.751 and 0.275	0.772 and 0.223	0.406 and 0.146	0.853 and 0.191	0.771 and 0.264	1 and 0.464	0.838 and 0.445	0.756 and 0.541
refinement method	full-matrix least-squares on F^2	full-matrix least-squares on F^2	full-matrix least-squares on F^2	full-matrix least-squares on F^2	full-matrix least-squares on F^2	full-matrix least-squares on F^2	full-matrix least-squares on F^2	full-matrix least-squares on F^2
data/restraints/parameters	1537/5/133	1556/3/133	1554/4/133	1554/4/133	1429/4/133	1460/5/133	1508/5/133	1405/5/133
goodness-of-fit on F^2	1.101	1.131	1.023	1.101	1.032	0.985	0.987	1.078
final R indices [$I > 2\sigma(I)$]	R_1 = 0.0278, wR_2 = 0.0700	R_1 = 0.0500, wR_2 = 0.1366	R_1 = 0.0472, wR_2 = 0.1043	R_1 = 0.0409, wR_2 = 0.1100	R_1 = 0.0297, wR_2 = 0.0637	R_1 = 0.0353, wR_2 = 0.0736	R_1 = 0.0297, wR_2 = 0.0560	R_1 = 0.0204, wR_2 = 0.0439
R indices (all data)	R_1 = 0.0307, wR_2 = 0.0713	R_1 = 0.0549, wR_2 = 0.1393	R_1 = 0.0653, wR_2 = 0.1140	R_1 = 0.0437, wR_2 = 0.1123	R_1 = 0.0345, wR_2 = 0.0660	R_1 = 0.0428, wR_2 = 0.0776	R_1 = 0.0378, wR_2 = 0.0575	R_1 = 0.0222, wR_2 = 0.0446
absolute structure parameter	−0.03(3)	−0.02(1)	−0.001(13)	−0.04(8)	−0.004(10)	−0.03(2)	−0.02(2)	−0.02(2)
largest diff peak and hole/e $Å^{-3}$	0.82 and −0.60	2.02 and −1.11	0.83 and −1.03	1.22 and −1.10	0.55 and −0.64	0.65 and −0.52	0.57 and −0.64	0.47 and −0.64

dx.doi.org/10.1021/ic202020z | Inorg. Chem. 2012, 51, 1703−1716

Table 1. continued

compound	11	12	13	14	15	16	17	18
identification code	Za4	Za6	Za8	Za10	Za12	Za14	Za16	Za18
empirical formula	C18 H16 Sm Na O12	C18 H16 Eu Na O12	C18 H16 Gd Na O12	C18 H16 Tb Na O12	C18 H16 Dy Na O12	C18 H16 Ho Na O12	C18 H16 Er Na O12	C18 H16 Yb Na O12
formula weight/g mol^{-1}	597.66	599.27	604.55	606.23	609.8	612.23	614.56	620.34
temperature/K	293(2)	293(2)	293(2)	293(2)	293(2)	293(2)	293(2)	293(2)
wavelength/Å	1.54184	1.54184	1.54184	1.54184	1.54184	1.54184	1.54184	1.54184
crystal system	orthorhombic	orthorhombic	orthorhombic	orthorhombic	orthorhombic	orthorhombic	orthorhombic	orthorhombic
space group	$C222_1$	$C222_1$	$C222_1$	$C222_1$	$C222_1$	$C222_1$	$C222_1$	$C222_1$
unit cell dimensions								
a (Å)	6.9094(2)	6.8969(4)	6.89120(10)	6.8767(2)	6.8673(2)	6.8571(2)	6.8454(2)	6.8290(1)
b (Å)	39.2050(8)	39.176(2)	39.1425(5)	39.1054(14)	39.0815(9)	39.0412(13)	39.0033(10)	38.9781(6)
c (Å)	7.5963(2)	7.5752(4)	7.55970(10)	7.5359(3)	7.5196(2)	7.4984(2)	7.4816(2)	7.4568(1)
cell volume/ $Å^3$	2057.7(1)	2046.8(2)	2039.15(5)	2026.5(1)	2018.1(1)	2007.4(1)	1997.5(1)	1984.86(5)
Z	4	4	4	4	4	4	4	4
calc density/mg m^{-3}	1.929	1.945	1.969	1.987	2.007	2.026	2.043	2.076
absorption coefficient/mm^{-1}	22.24	22.75	21.86	17.98	20.64	8.19	8.65	9.56
$F(000)$	1172	1176	1180	1184	1188	1192	1196	1204
crystal size (mm^3)	0.01 × 0.04 × 0.25	0.01 × 0.02 × 0.19	0.03 × 0.09 × 0.12	0.01 × 0.02 × 0.22	0.01 × 0.03 × 0.17	0.01 × 0.01 × 0.12	0.01 × 0.02 × 0.21	0.02 × 0.03 × 0.20
theta range for data collection/°	3.38−70.37	4.51−70.62	4.52−70.57	3.38−70.30	4.53−73.35	4.53−71.83	4.53−70.51	4.54−70.47
index ranges	$-8 \le h \le 7$	$-8 \le h \le 8$	$-7 \le h \le 8$	$-8 \le h \le 8$	$-7 \le h \le 8$	$-7 \le h \le 8$	$-8 \le h \le 8$	$-7 \le h \le 8$
	$-47 \le k \le 47$	$-43 \le k \le 47$	$-38 \le k \le 47$	$-47 \le k \le 34$	$-48 \le k \le 47$	$-47 \le k \le 42$	$-47 \le k \le 46$	$-47 \le k \le 35$
	$-7 \le l \le 9$	$-9 \le l \le 9$	$-9 \le l \le 9$	$-8 \le l \le 6$	$-6 \le l \le 9$	$-9 \le l \le 7$	$-9 \le l \le 8$	$-9 \le l \le 3$
reflections collected	5933	5895	9182	3722	3871	3900	5476	4026
independent reflections	1958 [R(int) = 0.03]	1951 [R(int) = 0.05]	1960 [R(int) = 0.03]	1874 [R(int) = 0.04]	1991 [R(int) = 0.03]	1943 [R(int) = 0.03]	1901 [R(int) = 0.05]	1886 [R(int) = 0.03]
completeness to $theta_{max}$ (%)	99.40	99.80	99.90	99.10	99.60	99.60	99.70	99.80
absorption correction	refined (XABS2)	refined (XABS2)	refined (XABS2)	refined (XABS2)	refined (XABS2)	refined (XABS2)	refined (XABS2)	refined (XABS2)
max and min transmission	1 and 0.288	0.721 and 0.450	0.538 and 0.186	1 and 0.944	0.851 and 0.264	0.953 and 0.627	1 and 0.928	0.742 and 0.493
refinement method	full-matrix least-squares on F^2	full-matrix least-squares on F^2	full-matrix least-squares on F^2	full-matrix least-squares on F^2	full-matrix least-squares on F^2	full-matrix least-squares on F^2	full-matrix least-squares on F^2	full-matrix least-squares on F^2
data/restraints/parameters	1958/5/161	1951/3/161	1960/4/161	1960/4/161	1991/5/161	1943/4/161	1901/5/161	1886/5/161
goodness-of-fit on F^2	1.041	1.058	1.083	0.934	1.085	1.083	1.023	1.061
final R indices [$I > 2\sigma(I)$]	$R_1 = 0.0181$, $wR_2 = 0.0412$	$R_1 = 0.0314$, $wR_2 = 0.0701$	$R_1 = 0.0152$, $wR_2 = 0.0369$	$R_1 = 0.0282$, $wR_2 = 0.0563$	$R_1 = 0.0302$, $wR_2 = 0.0802$	$R_1 = 0.0304$, $wR_2 = 0.0766$	$R_1 = 0.0299$, $wR_2 = 0.0667$	$R_1 = 0.0273$, $wR_2 = 0.0681$
R indices (all data)	$R_1 = 0.0196$, $wR_2 = 0.0417$	$R_1 = 0.0357$, $wR_2 = 0.0732$	$R_1 = 0.0153$, $wR_2 = 0.0370$	$R_1 = 0.0355$, $wR_2 = 0.0575$	$R_1 = 0.0325$, $wR_2 = 0.0816$	$R_1 = 0.0347$, $wR_2 = 0.0780$	$R_1 = 0.0342$, $wR_2 = 0.0688$	$R_1 = 0.0297$, $wR_2 = 0.0694$
absolute structure parameter	−0.02(1)	−0.03(1)	−0.006(3)	−0.013(7)	−0.001(8)	−0.03(1)	−0.04(2)	−0.03(2)
largest diff peak and hole/ $e·Å^{-3}$	0.46 and −0.28	0.54 and −0.55	0.44 and −0.36	0.91 and −0.65	0.73 and −1.23	0.98 and −0.39	0.90 and −0.70	2.19 and −0.53

dx.doi.org/10.1021/ic202020z | Inorg. Chem. 2012, 51, 1703−1716

Catalysis Studies. The procedure established for acetalization of benzaldehyde with trimethylorthoformate (TMOF) is described as follows: TMOF (5 mmol, 0.5 mL) and benzaldehyde (0.5 mmol, 0.05 mL) were added to a suspension of the catalyst (0.01 mmol) in 3 mL of tetrachloromethane. The reaction was carried out in a sealed tube under nitrogen atmosphere, mild conditions (70 °C), and magnetic stirring. Samples were taken at intervals and analyzed by gas chromatography.

Photoluminescence Studies. The photoluminescence spectra in the visible and NIR spectral ranges were recorded at room temperature with a modular double grating excitation spectrofluorimeter with a TRIAX 320 emission monochromator (Fluorolog-3, Horiba Scientific) coupled to a R928 and H9170 Hamamatsu photomultipliers, respectively, using the front face acquisition mode. The excitation source was a 450 W Xe arc lamp. The emission spectra were corrected for detection and optical spectral response of the spectrofluorimeter and the excitation spectra were corrected for the spectral distribution of the lamp intensity using a photodiode reference detector. The time-resolved measurements were acquired with the setup above-described for the photoluminescence spectra using a pulsed Xe–Hg lamp (6 μs pulse at half width and 20–30 μs tail). The NIR emission and excitation spectra were acquired with 20–50 scans.

RESULTS AND DISCUSSION

Single-crystal X-ray diffraction analyses reveal that all the compounds crystallize in the orthorhombic chiral space group $C222_1$, and the compounds of each series (**S1** or **S2**) are isostructural, tuned by the influence of the Ln^{3+} cations (see Table 1). The variation of unit cell parameters show dependency on the Shannon's effective ionic radii,[63] and the expected tendencies are observed: the ionic radii decrease linearly as the unit cell parameters (*a*, *b*, *c*, and volume) and distances Ln–Na do. These tendencies are illustrated in Figure 1. The coordination modes of carboxylate groups of $Tart^{2-}$, BDC^{2-}, and $biBDC^{2-}$ ligands in **S1** and **S2** are shown in Figure 3g. To the best of our knowledge, these coordination modes are uncommon and have not yet been reported.

The structures of the compounds of both series **S1** and **S2** consist of infinite chains, along the *a*-axis, of alternating $\{LnO_8\}$ and $\{NaO_6\}$ polyhedra edge-shared through two carboxylate oxygen atoms, O(1) (from BDC^{2-} or $biBDC^{2-}$) and O(4) (from $Tart^{2-}$). The distance between adjacent Ln–Na cations in the chain, from the beginning to the end of **S1** and **S2**, ranges from 3.861(1) Å (for **Za3**, Sm) to 3.798(1) Å (for **Za17**, Yb), and from 3.849(1) Å (**Za4**, Sm) to 3.786(1) Å (**Za18**, Yb), with the average values of 3.831 Å and 3.820 Å, respectively. The flexible $Tart^{2-}$ ligand serves as a bridge to link the ···Ln–Na–Ln–Na··· chains along the *a*- and *c*-axis to create a double layer in a zigzag fashion, while the rigid BDC^{2-} in **S1** or $biBDC^{2-}$ ligands in **S2** are parallel to the *b*-axis and act as pillars separating two successive double layered networks, resulting in isoreticular layered chiral Ln/Na-organic frameworks (Figure 2). The distance centroid-to-centroid between neighboring BDC^{2-} ligands in **S1** or $biBDC^{2-}$ in **S2** along the *c*-axis ranges, respectively, from 3.83 Å (for **Za3**) to 3.78 Å (for **Za17**), and from 3.84 Å (**Za4**) to 3.80 Å (**Za18**), thus indicating the possibility of weak noncovalent π–π interactions, which is an offset stacking, where the ring normal forms an angle of about 10° with the vector between the rings centroids. In the case of **S2**, $biBDC^{2-}$ is not planar and has a torsion angle ranging from a maximum value of 36.61° (for **Za4**) to minimum of 34.13° (for **Za18**). The slight decrease in the centroid-to-centroid distance, as well as the torsion angle in the case of **S2**, shows a dependency on the ionic radii of Ln^{3+} cations. The spacers BDC^{2-} in **S1** or $biBDC^{2-}$ in **S2** are one-sided coordinated and bind three cations (one Ln^{3+} and two Na^{+}) in a tetradentate chelating–bridging mode ($\mu^3 - \eta^1$: η^2: η^1). However, the opposite side is involved in strong hydrogen bond interactions between the oxygen atoms O2 of the noncoordinated carboxylate groups O2–C6–O2 of the BDC^{2-} ligand in **S1**, or O2–C10–O2 of the $biBDC^{2-}$ ligand in the case of **S2**, which acts as an acceptor, and the oxygen atom O3 of the hydroxyl groups of the $Tart^{2-}$ ligand, together with the coordinated water molecules O6 to the sodium atom which act as donors, therefore imparting 3D stability to the structure. The unusual coordination mode of BDC^{2-} ($biBDC^{2-}$ in the case of **S2**), in a successive switch manner, gives rise to an undulating interlayer surface propagating in the *a*- and *c*-directions. Both series of compounds contain one Ln^{3+} and Na^{+} cation crystallographically independent, each with half occupancy sitting on a 2-fold crystallographic axis along the *b*-direction. Around each Ln^{3+} cation are eight oxygen atoms (Figure 3a,c), six of them carboxylic (O1 form BDC^{2-} or $biBDC^{2-}$, and O4 and O5 from $Tart^{2-}$) and two from hydroxyl groups (O3 from $Tart^{2-}$). Its coordination geometry may be described as a distorted bicapped trigonal-prism (Figure 3b), while the Na^{+} cation is bonded to six oxygen atoms (Figure 3d,f), four of them carboxylic (O1 and O4) and two from coordinated water molecules (O6), and its geometry may be described as distorted trigonal prism (Figure 3e). Out of the eight oxygen atoms coordinated to Ln^{3+}, six come from four symmetry-related $Tart^{2-}$ anions: two of them are coordinated to Ln^{3+} in chelating modes via the carboxylic oxygen atom O5 and the hydroxyl oxygen atom O3, and the last two act as a bridge between the Ln^{3+} and Na^{+} through the carboxylic oxygen atom O4. The two remaining oxygen atoms bonded to Ln^{3+} belong to one BDC^{2-} anion in **S1** or $biBDC^{2-}$ in the case of **S2**, which acts (i) in chelating mode via the carboxylate group O1–C1–O1 and (ii) in bridging mode between Ln^{3+} and Na^{+} within each carboxylate oxygen atom O1. Out of the six oxygen atoms coordinated to Na^{+}, two come from the $Tart^{2-}$ anion which acts in chelating mode via the carboxylate oxygen atoms O4, and the four remaining, every two of them belong to two symmetry-related: (i) coordinated water molecules, (ii) BDC^{2-} anions (or $biBDC^{2-}$ anions in the case of **S2**), by coordinating oxygen atoms O6 and O1, respectively. In **S1**, the distances Ln–O and Na–O range from a maximum average value of 2.408 Å and 2.434 Å (for **Za3**, Sm) to minimum average values of 2.315 (3) Å and 2.407 Å (for **Za17**, Yb). Similarly, the pertinent values in **S2** range from 2.405 Å and 2.431 Å (for **Za4**, Sm) to 2.319 Å and 2.406 Å (for **Za18**, Yb), respectively, which are usual values for oxygen-coordinated lanthanides or sodium atoms compounds with carboxylic acids.

The series of compounds **S1** and **S2** display very similar IR spectra as depicted in Figure S3 (see Supporting Information). The strong and broad adsorption bands in the region 3600–3400 cm^{-1} are attributed to the characteristic O–H stretching vibrations from hydroxyl groups of $Tart^{2-}$ ligands and coordinated water molecules to sodium atoms; the existence of these two different types of chemical species is evident in the spectra which show two markedly distinct bands at ca. 3590 cm^{-1} and 3470 cm^{-1} assigned, respectively, to water molecules and hydroxyl groups. The two weak bands at ca. 3065 cm^{-1} are assigned to =C–H stretching vibrations of phenylene rings of BDC^{2-} or $biBDC^{2-}$ ligands, and those at ca. 2960 cm^{-1} and 2920 cm^{-1} are attributed to C–H stretching vibrations of the alkane chain of $Tart^{2-}$ ligand. The two coordination modes adopted by the carboxylate groups of $Tart^{2-}$, and

dx.doi.org/10.1021/ic202020z | *Inorg. Chem.* 2012, 51, 1703–1716

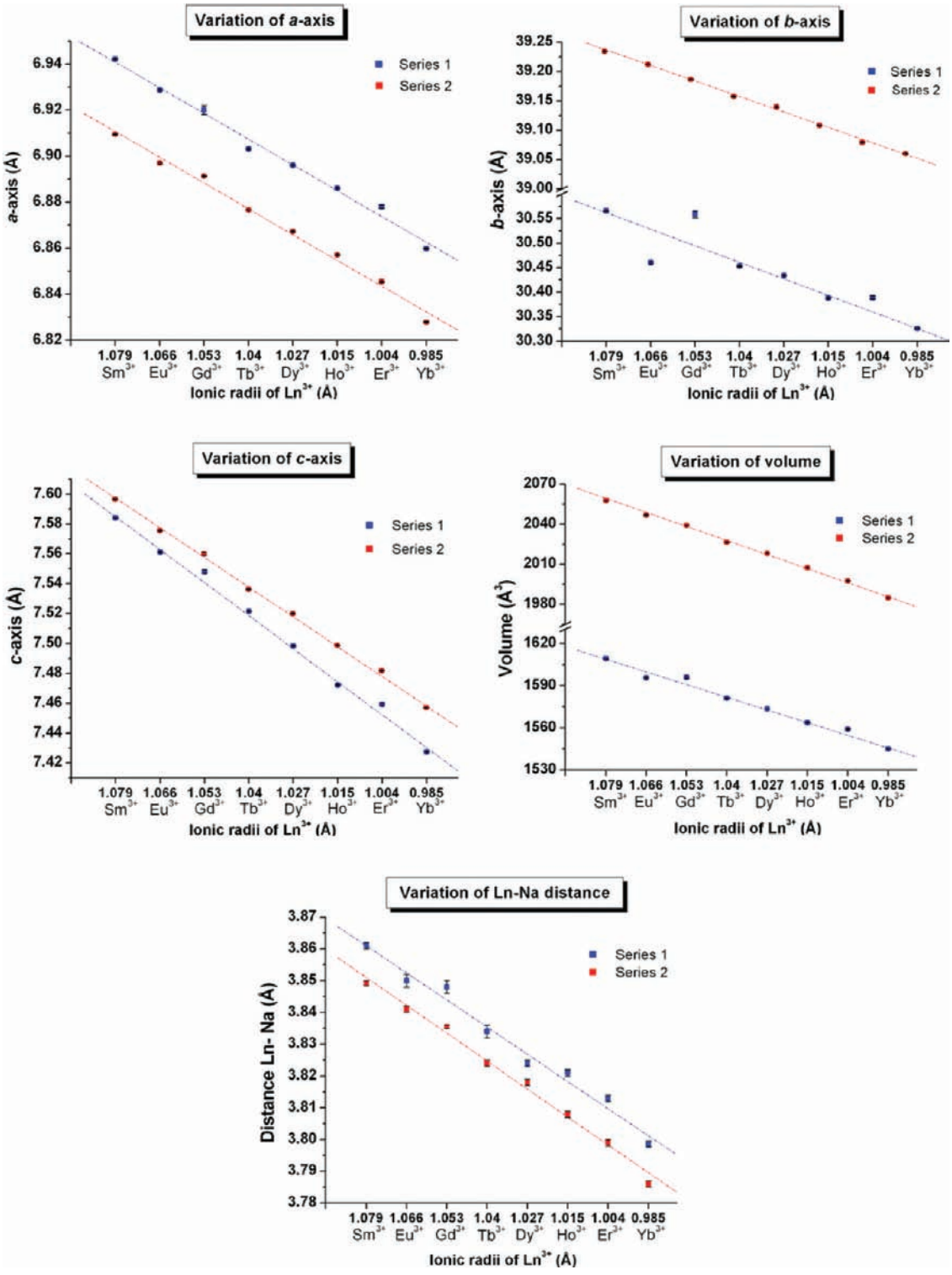

Figure 1. Variation of cell parameters (*a*, *b*, and *c*), volume, and Ln−Na distance vs Shannon's ionic radii (Å) of Ln^{3+} cations in the series of compounds **S1** and **S2**.

BDC^{2-} or $biBDC^{2-}$ ligands in all the compounds are clearly distinguished from the spectra. The characteristic bands for the asymmetric and symmetric stretching vibrations of the carboxylate groups appear at ca. 1640−1545 cm^{-1} and 1470−1360 cm^{-1}, respectively. The values of $\Delta\upsilon = \upsilon_{asym}(CO_2^-) - \upsilon_{sym}(CO_2^-)$ of ca. 140−180 cm^{-1} may confirm the bridging mode of the carboxylate groups found in these compounds. The band at 1670 cm^{-1} may be assigned to the uncoordinated and deprotonated carboxylate group of BDC^{2-} or $biBDC^{2-}$ involved in strong hydrogen bonds. The strong band at ca. 1510 cm^{-1} corresponds to C=C stretching vibrations (skeletal vibrations). Bands at ca. 1350 cm^{-1} and 1304 cm^{-1} may be assigned to O−H stretching vibrations of hydroxyl $Tart^{2-}$. The band at ca. 1242 cm^{-1} is attributed to C−O stretching vibrations of carboxylate groups. The bands corresponding to C−OH stretching vibrations of $Tart^{2-}$ appear at ca. 1074 cm^{-1}. The band at ca. 865 cm^{-1} may

dx.doi.org/10.1021/ic202020z | Inorg. Chem. 2012, 51, 1703−1716

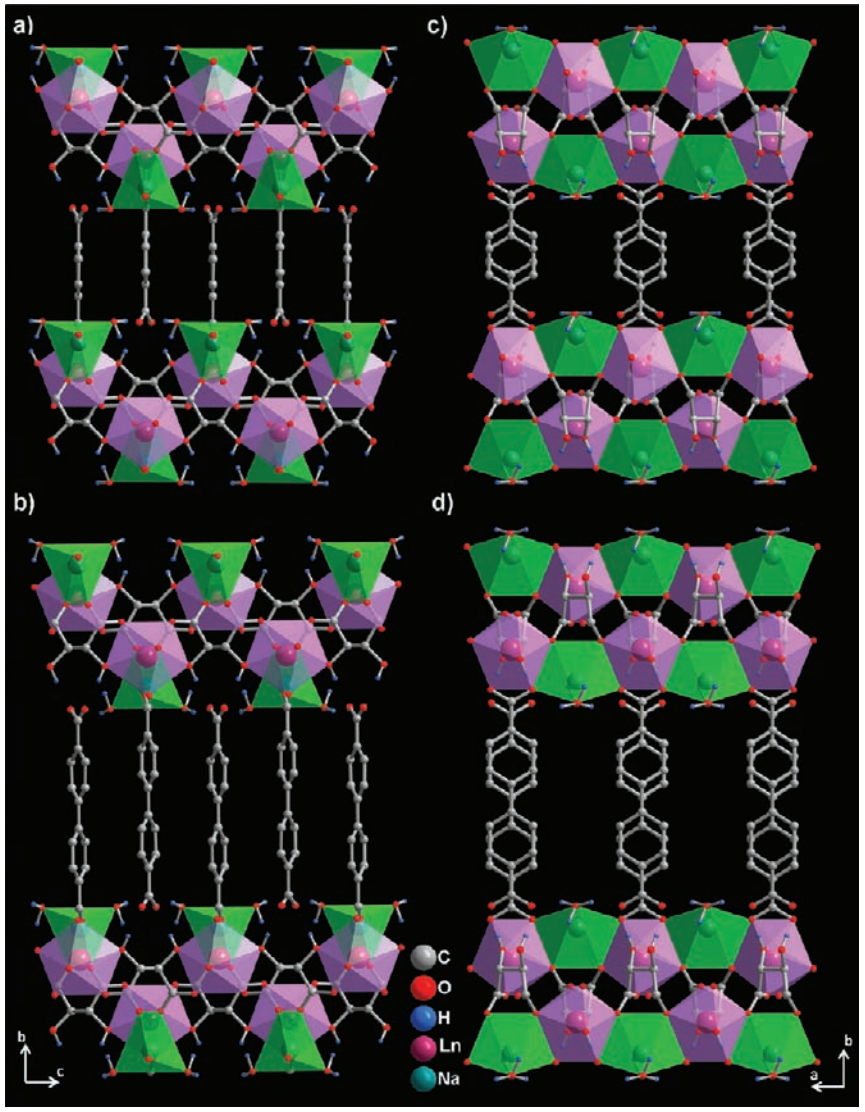

Figure 2. Projection of the structure of compounds **S1** (a, c) and **S2** (b, d) along the *a*- and *c*-axis. C−H hydrogen atoms have been omitted for clarity.

be attributed to scissoring vibrations of carboxylate groups. The aromatic =C−H out-of-plane deformation vibrations are confirmed by the strong bands at ca. 798 cm^{-1} (strong) and 710 cm^{-1} (weak). The band corresponding to C−C−O stretching vibrations of $Tart^{2-}$ appear at ca. 740 cm^{-1}. Bands at ca. 534 cm^{-1} and 424 cm^{-1} may be assigned, respectively, to in-plane rocking vibration and out-of-plane of deformation vibrations of carboxylate groups bonded to aromatic rings. The main difference between **S1** and **S2** is the fact that in **S2** an additional sharp strong band appeared centered around 690 cm^{-1} which is due to C−H out-of-plane deformation vibrations arising from the second aromatic ring of $biBDC^{2-}$.[64−66]

The thermal stability in air of **S1** and **S2** was investigated. Comparison TG curves for the series of compounds **S1** or **S2** are depicted in Figure S4 (see Supporting Information), respectively. For each compound, the TG/DTG/SDTA curves with the corresponding mass spectrometry analysis are provided in Figure S5, while Figure S6 shows DSC traces (see Supporting Information). The final product was identified as an equal (1:1) mixture of Ln_2O_3 (detected by PXRD) and amorphous Na_2O (by EDX microanalysis), and coal (by C−H−N elemental analysis). The TG curves of **S1** and **S2** very closely resemble each other and reveal the observed total mass losses, presented in Table S4 (see Supporting Information), from room temperature up to 1000 °C.

In the case of **S1**, **Za9** has been taken as a representative example. As shown in Figure S5d (see Supporting Information), the thermal decomposition process of **Za9** proceeds in five stages. The first mass loss between 140 and 260 °C with the total mass loss of 6.5% (cal. 6.79%) corresponds to the gradual loss of the two water molecules coordinated to the sodium atom. The rest of the stages, from the second to the fifth in the range 270−560 °C, are continuous and overlapping with the total mass loss of ca. 48.2%, assigned to a complex decomposition process of the mixed-ligands. Additional mass loss of ca. 2% has been observed in the range 950−1000 °C, which is assigned to the liberation of some trapped organic part after the structure collapse. The associated mass spectrometry *m*/*z* 18 (H_2O) and *m*/*z* 44 (CO_2) curves are in good agreement with TG/DTG curves. Taking into account that the mass spectrometry analysis is a semiquantitative method, the integration of the first band (608 nA) is almost half of the

dx.doi.org/10.1021/ic202020z | *Inorg. Chem.* 2012, 51, 1703−1716

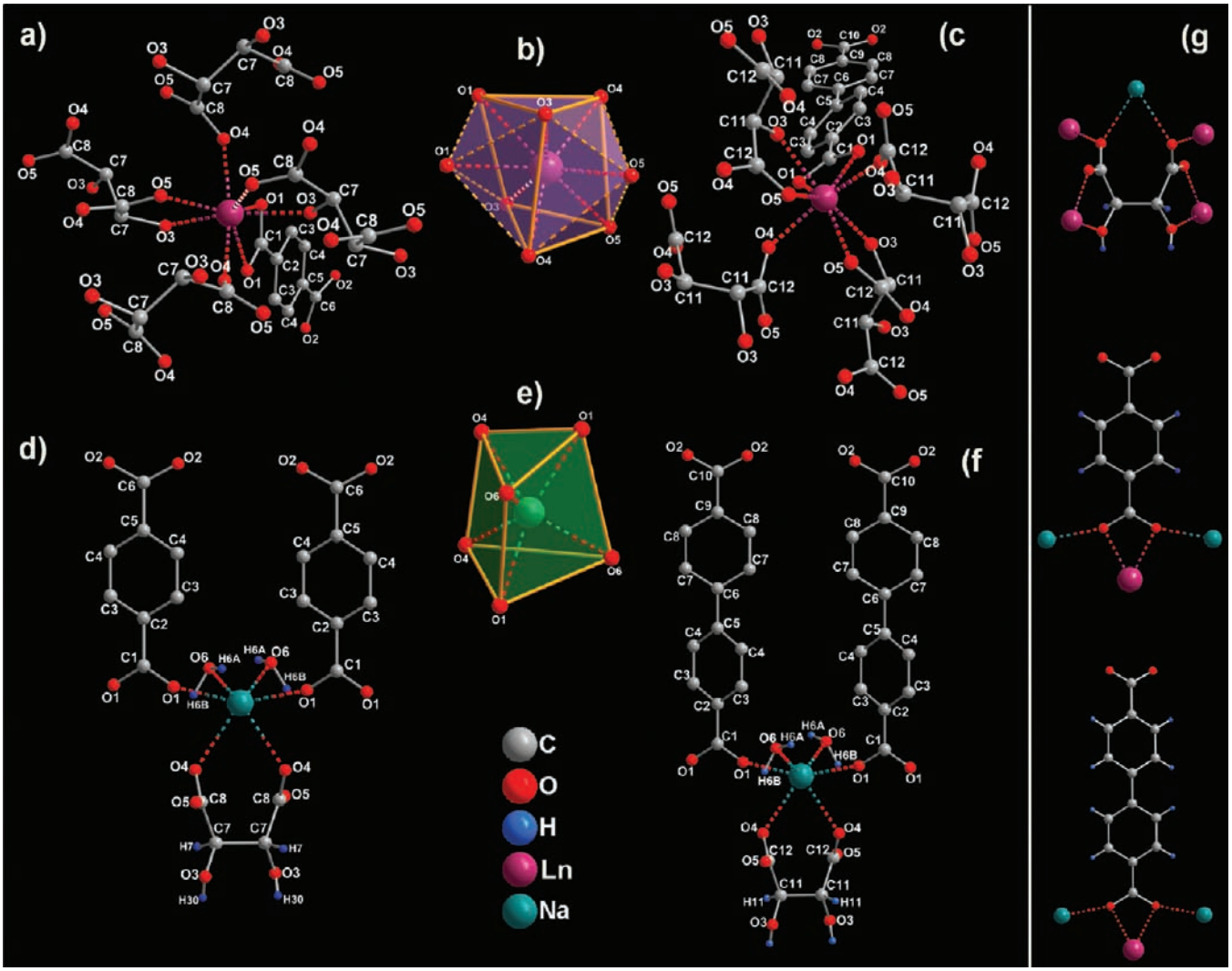

Figure 3. Perspective view of the coordination environment of Ln^{3+} in **S1** (a, b) and **S2** (b, c), and Na^{+} in **S1** (d, e) and **S2** (e, f). Coordination modes of $Tart^{2-}$, BDC^{2-}, and $biBDC^{2-}$ ligands (g).

integration of the second, third, and fourth ones (1367 nA) in the m/z 18 curve, indicating the loss of approximately four water molecules in the second, third, fourth, and fifth steps, corresponding to the amount of hydrogen atoms resulting from the decomposition of both $Tart^{2-}$ and BDC^{2-} ligands in the formula of **Za9**.

In the same way, **Za10** is taken as a representative example of **S2** (Supporting Information, Figure S5d). **Za10** undergoes five steps of mass loss; the first step (exp. 5.6%) at 150−240 °C corresponds to the loss of coordinated water molecules (calcd. 5.94%). The rest of the steps (exp. 54.5%; calcd. 58.77%) in the range 290−540 °C are continuous and overlapping, and correspond to the progressive decomposition of the ligands. Additional mass loss (ca. 2%) between 900−1000 °C is attributed to the liberation of some trapped organic moieties after the structure collapse. The associated mass spectrometry m/z 18, m/z 44, and m/z 78 (C_6H_6) curves are in agreement with those of TG/DTG. m/z 78 (C_6H_6) curve has one maximum (450 °C) and shows that the decomposition of $biBDC^{2-}$ ligand starts basically in the fourth stage, manifested by the contraction of interlayer spacing from ca. 18.8 Å (of dehydrated phase of **Za10**) to ca. 14.7 Å (confirmed by powder X-ray thermodiffraction studies; see violet powder pattern at 450 °C in Figure S7 in Supporting Information) due to the loss of one phenyl group of $biBDC^{2-}$ ligand. In the m/z 18 curve, the integration of the first band (440 nA) is almost a third of the integration of the second, third, and fourth ones (1296 nA), which proves the loss of approximately six water molecules in the second, third, fourth, and fifth stages, corresponding to the hydrogen atoms resulting from the decomposition of the both $Tart^{2-}$ and $biBDC^{2-}$ ligands in the formula of **Za10**.

For the remaining compounds of **S1** and **S2**, numerical values of TG-DTG-MS and SDTA/DSC curves are represented in Table S4 (see Supporting Information). To summarize, the first stage is attributed to the release of two coordinated water molecules, the second stage corresponds to the loss of $Tart^{2-}$ fragments followed by combustion, the third stage is shared between the continuation of $Tart^{2-}$ combustion and the beginning of BDC^{2-} or $biBDC^{2-}$ combustion, and finally, the fourth and fifth stages are dominated by the combustion and loss of phenyl groups of BDC^{2-} or $biBDC^{2-}$.

In addition, the dehydration enthalpies for **S1** and **S2**, ranging from −36 kJ/mol to −105 kJ/mol and −34 kJ/mol to −107 kJ/mol, respectively, are fairly close and comparable. However, oxidative decomposition enthalpies are found to be higher in **S2** than **S1**, varying in the ranges 3571−6690 kJ/mol

dx.doi.org/10.1021/ic202020z | *Inorg. Chem.* 2012, 51, 1703−1716

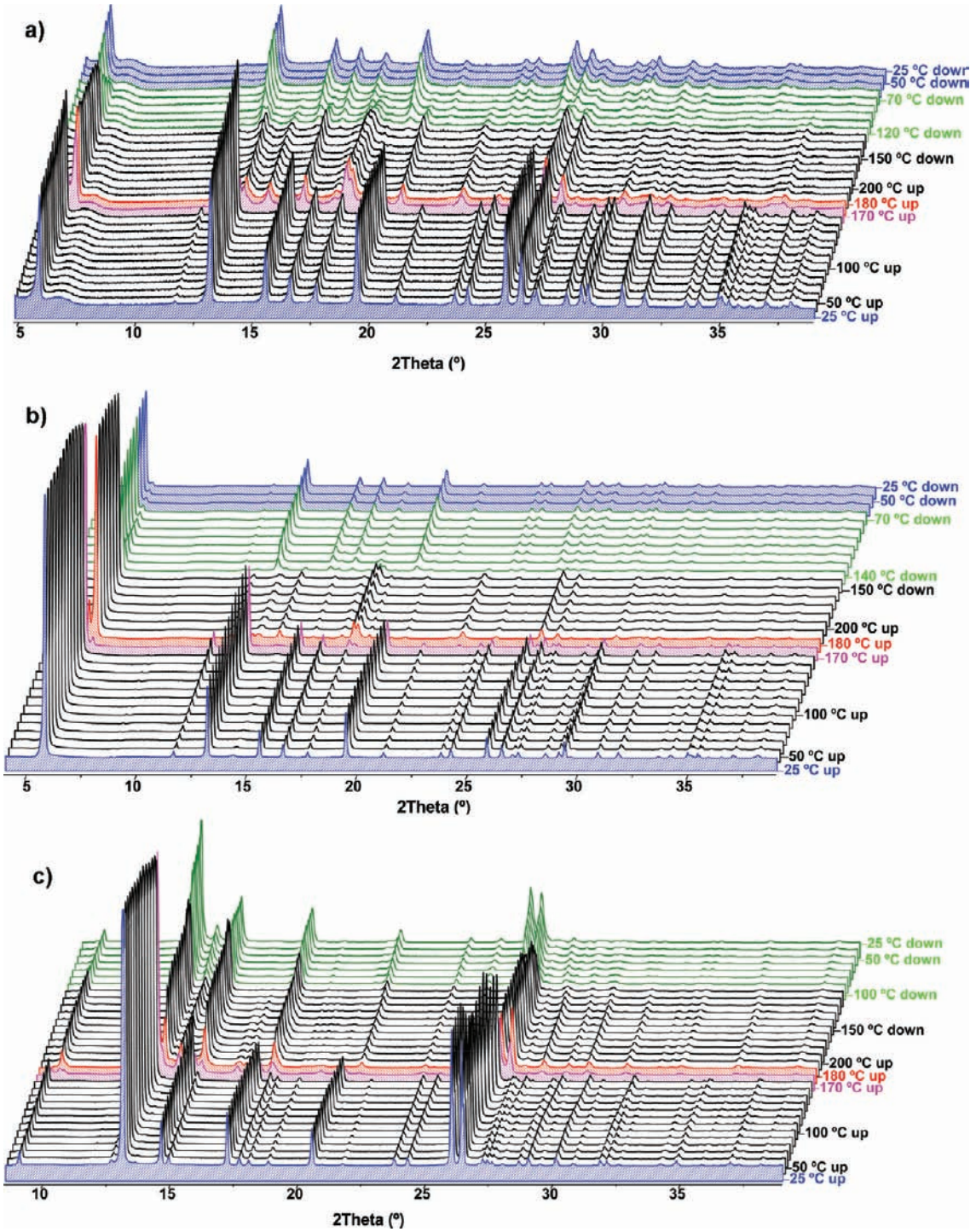

Figure 4. X-ray thermodiffractogram of **Za7** (a), **Za13** (b), and **Za16** (c) recorded in air heating up from 25 to 200 °C and cooling down to 25 °C. Color code corresponding to the structural changes, blue: **Za7**, **Za13**, or **Za16**, pink: dehydration of **Za7**, **Za13**, or **Za16**, red: dehydrated **Za7**, **Za13**, or **Za16**, green: rehydration **Za7**, **Za13**, or **Za16**, blue: rehydrated **Za7** or **Za13**.

and 2051−3889 kJ/mol, respectively, which is related to the difference between oxidative decomposition enthalpies of BDC^{2-} and $biBDC^{2-}$, estimated at ca. 2200 kJ/mol.

The X-ray thermodiffraction analysis carried under air heating up from 25 to 200 °C and cooling down to 25 °C were performed for **Za7**, **Za13**, and **Za16** (see Figure 4, panels a, b, and c, respectively), and under vacuum heating up from room temperature to 900 °C for **Za16** (Figure S7, Supporting Information). The results confirm that **S1** and **S2** exhibit a phase transformation corresponding to the dehydration process by losing the two water molecules coordinated to sodium atoms, which is a reversible process for **S1**, involving a spontaneous rehydratation after cooling down to room temperature, clearly illustrated by thermodiffractogram of **Za7** and **Za13** (blue powder patterns at 25 °C down, Figure 4a,b). However, rehydratation is slowly reversible in the case of **S2** illustrated by thermodiffractogram of **Za16** (green powder patterns on Figure 4c) and estimated to be approximately half rehydrated at the end of the experiment (confirmed by TG analysis).

dx.doi.org/10.1021/ic202020z | *Inorg. Chem.* 2012, 51, 1703−1716

For **Za7**, **Za13**, or **Z16**, no structural change occurs below 160 °C, and no significant change in the unit cell parameters has been observed. The phase transformation to the anhydrous form begins at 170 °C, and the total transformation to the anhydrous form is reached at 180 °C and maintained until 200 °C, which is consistent with the TG analyses. During the temperature decrease the anhydrous phase is preserved, and the rehydration begins at 120 °C, 140 °C, and 100 °C for **Za7**, **Za13**, and **Z16**, respectively, and continues until room temperature. The patterns of dehydrated compounds of **Za7** and **Za13** correspond to the as-synthesized compounds with some diffraction intensity drop and peak broadening. In contrast with **S1** compounds, the rehydration of **S2** compounds (**Za16**) is not achieved at the end of the experiment, and takes a few days in air, indicating the slow reversibility of the process.

X-ray thermodiffractogram of **Za16** under vacuum heating up to 900 °C (see Figure S7, Supporting Information) indicates no structural change below 100 °C. At 150 °C the dehydrate phase appears and progressively increases until reaching the total transformation at 250 °C, and the anhydrous phase is preserved until 300 °C. At 350 and 400 °C, powder patterns show a broad peak at $2\theta \sim 5.4°$ corresponding to the interlayer distance, and practically no other diffraction peaks have been observed at higher angles, which is due to phase amorphization caused by decomposition of the organic ligands. At 450 and 500 °C, the broad peak became sharp, its intensity markedly increases, and is shifted toward higher angles due to contraction of the interlayer spacing from ca. 18.8 Å (of dehydrated phase) to ca. 14.7 Å caused by loss of phenyl groups; moreover, a second peak corresponding to the interlayer distance at $2\theta \sim 11.8°$ also appears. This behavior is explained by the fact that the decomposition of $Tart^{2-}$ (incorporated in the layer) is stopped and loss of phenyl groups of $biBDC^{2-}$ (pillaring the layers) is continued. Above 550 °C, practically no diffraction peak has been observed due to the structure collapse. These results are consistent with TG analyses. However, a new phase has been formed characterized by a series of broad diffraction peaks corresponding to the formation of Er_2O_3.

X-ray powder diffraction patterns of dehydrated forms for **Za7**, **Za13**, and **Za16** at 200 °C have been indexed in the orthorhombic system with the following unit cell parameters: $a = 6.818(2)$ Å, $b = 28.634(8)$ Å, $c = 7.297(5)$ Å, $V = 1424.5(6)$ Å^3, for **Za7**, $a = 6.7713(4)$ Å, $b = 28.728(2)$ Å, $c = 7.3292(8)$ Å, for **Za13**, and $a = 6.7357(6)$ Å, $b = 37.875(4)$ Å, $c = 7.5869(7)$ Å, $V = 1935.5(4)$ Å^3, for **Za16**. The results reveal the structure contraction of ca. 7% (for **Za7**), ca. 6% (**Za13**), and ca. 3% (**Za16**) along the *b*-axis, maintaining the orthorhombic symmetry, after the loss of two water molecules coordinated to the sodium atoms. The *a*- and *c*-axis are almost unchanged in all cases. The structural modeling of dehydrated forms have been previously reported for yttrium-based compounds.[67]

Two compounds **Za15** (based on Er) and **Za17** (based on Yb) of **S1** have been selected to test their catalytic activity to behave as Lewis acid catalysts in acetalization of benzaldehyde (Supporting Information, Figure S8a,b), and their catalytic activity has been compared with that of a yttrium-based compound (compound **1**) previously reported.[55] The results show that the catalytic activity is quite improved when the catalytic center is Yb or Er, although it takes place on the surface. The greater catalytic effect of a Yb-based compound (**Za15**) may be explained in terms of more acidic character when the ionic radii decrease. In order to check the stability and heterogeneity of these catalysts, four consecutive catalytic cycles have been carried out with **Za15** catalyst (Supporting Information, Figure S8c). The first reaction cycle was carried out until the conversion reaches 60% (ca. 48 h) using 0.02 mmol of catalyst. After each catalytic cycle, the reaction mixture was centrifugated, the organic phase was removed, and then fresh substrates and solvent were added without further addition of catalyst. A slight decrease in the catalytic activity (ca. 7%) after four reaction cycles is probably due to the loss of some amount of catalyst by manipulation. The solid catalyst withdrawn after the fourth cycles has been characterized by PXRD which proves its stability (see Supporting Information, Figure S8d). Moreover, to rule out the contribution of homogeneous catalysis due to a potential leaching of catalysts, the filtered liquid of the fourth reaction cycle was allowed to react; however, no further significant conversion (4%) was observed after ca. 48 h.

The series of compounds **S1** and **S2** have been examined under UV-light and they exhibit tunable color emission over the whole visible light range by changing the doping Ln^{3+} cation or its concentration, or the type of structure (**S1** or **S2**), as exemplified in Figure 5. For instance, the crystals of **Za5** display a red-light emission visible with the naked eye, as exemplified in Figure 5e,f. In order to monitor the excitation paths that induce such emission features, the excitation spectra were monitored within the Eu^{3+} $^5D_0 \rightarrow {}^7F_2$ transition (Figure 6). The spectra of **Za6** and **Za5** are very similar being formed of a large band with three peaks around 250 nm, 270 nm, and 310 nm ascribed to the excited states of the $biBDC^{2-}$ or BDC^{2-} ligands (Supporting Information, Figure S9) and of a series of straight lines ascribed to the intra4f^6 $^7F_{0,1} \rightarrow {}^5D_{4-1}, {}^5G_{2-6}, {}^5L_6$ transitions. The low-relative intensity of the intra4f^6 lines point out that the Eu^{3+} ion sensitization process is more efficient when compared with direct intra4f^6 excitation. The excitation paths in the presence of Gd^{3+} ions were also monitored for **DZa7** (synthesis, crystallographic data, and structural characterization for **DZa7** are given in Supporting Information), Figure 6. This spectrum resembles the ones acquired for the pure Eu^{3+} samples being, however, observed changes in the relative intensity of the broad band components and a decrease in the relative intensity of the intra4f^6 lines, which indicates a better Eu^{3+} sensitization process in the presence of Gd^{3+} ions. Nevertheless, the absence on Gd^{3+} lines in the excitation spectrum monitored within the Eu^{3+} emission lines indicates the absence of an efficient room-temperature Gd^{3+}-to-Eu^{3+} energy transfer mechanism. Figure 7 compares the emission features of **Za6**, **Za5**, and **DZa7** under excitation via the broad band (270 nm) and directly into the intra4f^6 levels (395 nm, $^5L_6$). The spectra are formed of the Eu^{3+} $^5D_0 \rightarrow {}^7F_{0-4}$ transitions, and for **Za6** a low-intensity broad band originated from the ligands excited states in which a series of intra4f^6 self-absorptions are superimposed is also detected. For **Za6** and **Za5** the presence of a single line for the nondegenerated $^5D_0 \rightarrow {}^7F_0$ transition, the Stark splitting into 2 and 3 clearly expresses that components for the $^5D_0 \rightarrow {}^7F_{1,2}$ transitions and the high relative intensity of the $^5D_0 \rightarrow {}^7F_2$ transition are in accord with the Eu^{3+} local site symmetry (C_2) determined based on the crystal structures. Moreover, the energy and full width at half-maximum (fwhm) of the intra4f^6 lines are almost independent of the excitation wavelength, in good agreement with the presence of a single average local environment for the Eu^{3+} in both crystals. Nevertheless, **Za6** emission lines display a higher fwhm value, when compared with that of **Za5**, as well exemplified by the fwhm value of the $^5D_0 \rightarrow {}^7F_0$ transition illustrated in the inset in Figure 7 (15.4 ± 0.4 and 26.6 ± 0.9 cm^{-1} for **Za5** and **Za6**, respectively). The presence of Gd^{3+} induces both an enlargement of the

dx.doi.org/10.1021/ic202020z | Inorg. Chem. 2012, 51, 1703–1716

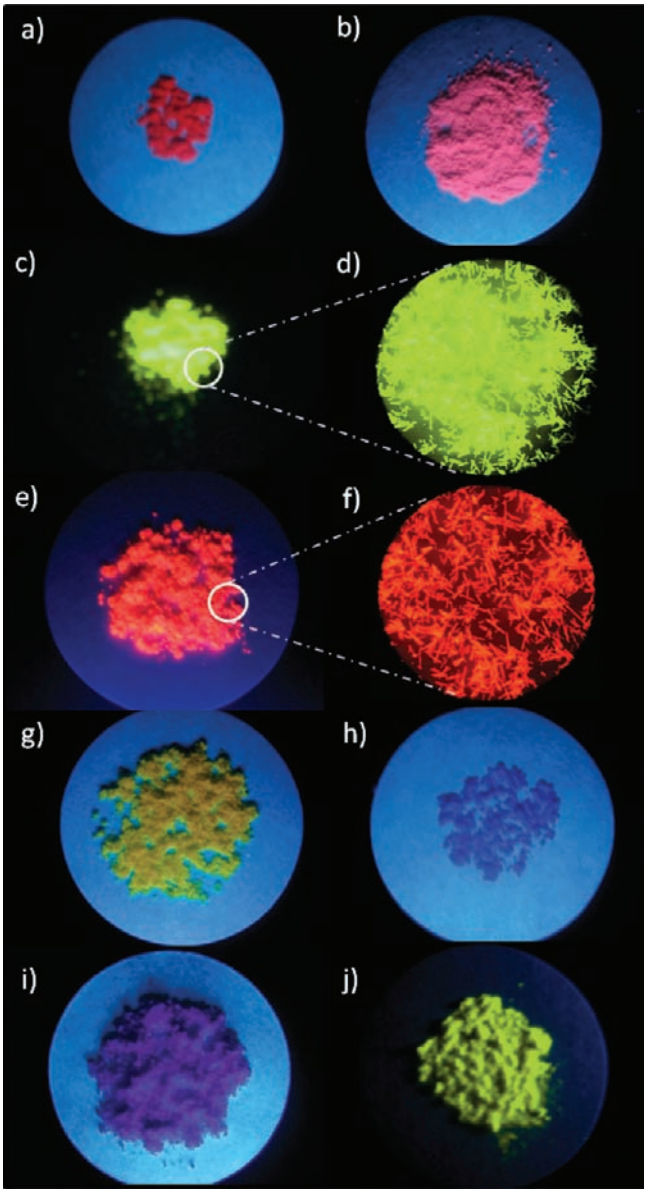

Figure 5. Digital photographs under UV radiation (254 nm) of **Za3**-red (a), **Za4**-pink (b), **Za9**-green (c, d), **Za5**-red (e, f), **Za11**-yellowish-orange (g), **Za12**-blue (h), **Za13**-deep-purple (i), and Tb-doped-Y-compound-yellow (j). Panels (d) and (f) were obtained by optical microscopy.

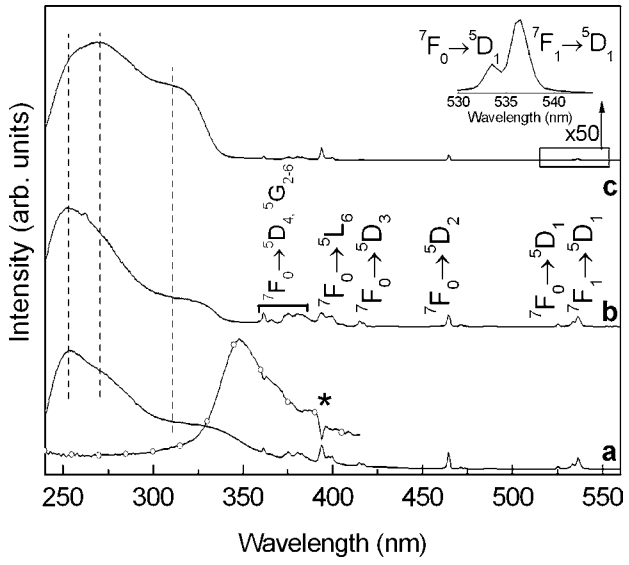

Figure 6. Excitation spectra of **Za6** (a), **Za5** (b), and **DZa7** (c) monitored within 616−618 nm. The spectrum of **Za6** monitored at 420 nm is also shown (solid line and open circles); the asterisk denotes the intra4f^6 self-absorption ascribed to the $^7F_0 \rightarrow {}^5L_6$

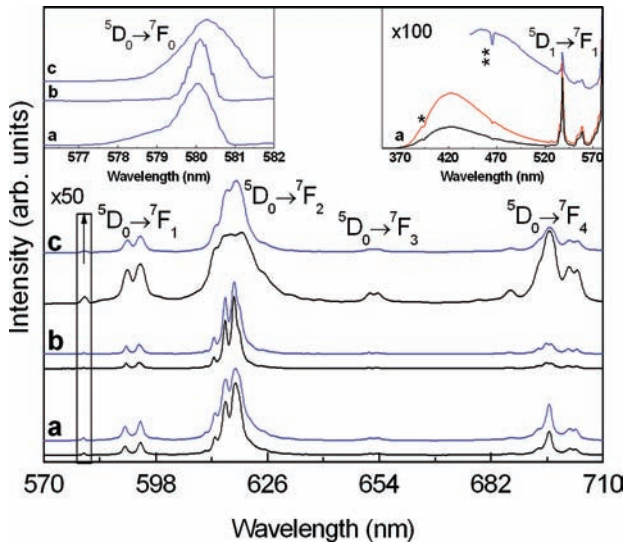

Figure 7. Emission spectra of **Za6** (a), **Za5** (b), and **DZa7** (c) under different excitation wavelengths. The insets show a magnification of

Eu^{3+} emission lines (e.g., 40.6 ± 1.0 cm^{-1} for the $^5D_0 \rightarrow {}^7F_0$ transition) and variations in the energy of the components, suggesting a larger distribution of Eu^{3+}similar local environments compared with that found in **Za6** and **Za5**. Moreover, the relative intensity of the $^5D_0 \rightarrow {}^7F_{0-4}$ transition depends on the excitation wavelength, reinforcing this assumption. The emission features of the three crystals were further quantified by the measurement of the $^5D_0$ decay curves monitored within the $^5D_0 \rightarrow {}^7F_2$ transition, under direct intra4f^6 excitation (395 nm, $^5L_6$), Figure 8. Whereas the emission of **DZa7** is well reproduced by a single exponential function yielding a lifetime value of 0.574 ± 0.002 ms, the emission decay curves of **Za6** and **Za5** display a rise-time behavior for time values below 1 ms (inset in Figure 8) probably ascribed to the contribution of the $^5D_1$ or ligands levels. For time values higher than 1 ms, the decay curves reveal a single exponential decay with lifetime values of 0.588 ± 0.002 ms and 0.608 ± 0.002 ms for **Za6** and **Za5**, respectively.

Figure 9a,b shows the emission spectra of Dy^{3+}-based materials under distinct excitation wavelengths. The spectra of **Za12** are formed of a high-relative intensity broad band (380−500 nm) and a series of Dy^{3+} lines attributed to the $^4F_{9/2} \rightarrow {}^6H_{15/2-11/2}$ transitions. For **Za11** the emission is characterized by a low-relative intensity broad band (380−650 nm) and by the typical Dy^{3+} $^4F_{9/2} \rightarrow {}^6H_{15/2-11/2}$ transitions. The large broad band in each sample can be ascribed to the excited states of the BDC^{2-} or $biBDC^{2-}$ ligands (Supporting Information, Figure S9). The excitation spectra were selectively monitored within the large broad band (410−450 nm) and within the Dy^{3+} emission lines (575 nm), as exemplified in the inset of Figure 9a,b for **Za12** and **Za11**, respectively. The latter spectrum reveals a broad band (240−380 nm)

dx.doi.org/10.1021/ic202020z | *Inorg. Chem.* 2012, 51, 1703−1716

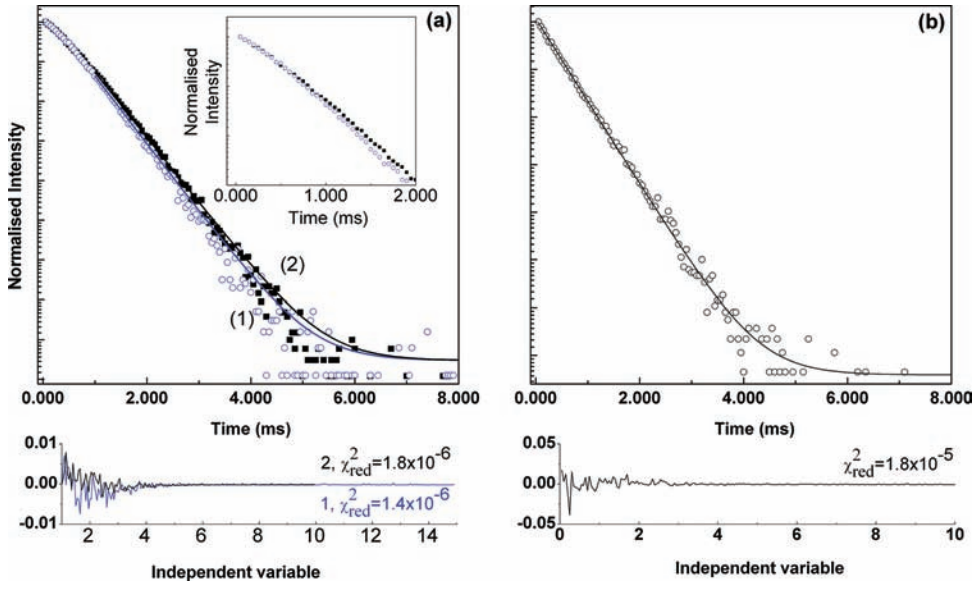

Figure 8. Emission decay curves of **Za6** (1, pen circles) and **Za5** (2, solid squares) (a) and of **DZa7** monitored at 616 nm and excited at 395 nm (b). The solid lines represent the data best fit using a single exponential function. The respective residual plots and the reduced-χ^2 (χ^2_{red}) values are also shown for a better judgment of the fit quality.

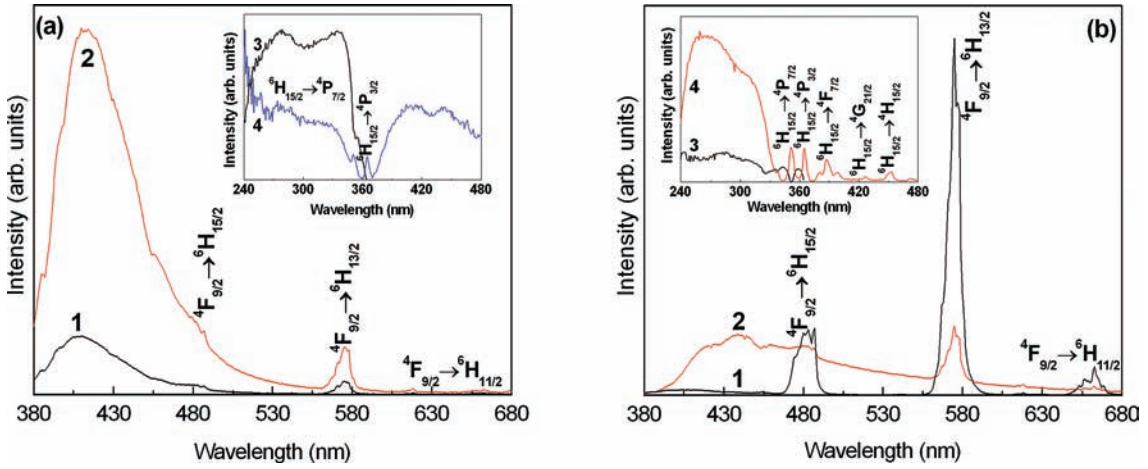

Figure 9. Emission spectra of **Za12** (a) and **Za11** (b) excited at (1) 270 nm, (2) 340−350 nm. The insets show the excitation spectra monitored at (3) 410 nm and (4) 575 nm.

superimposed on a series of Dy^{3+}-related lines assigned to the $^6H_{15/2} \rightarrow {}^4P_{7/2,3/2}$, $^4F_{7/2}$, $^4G_{21/2}$, $^4P_{7/2,3/2}$, and $^4H_{15/2}$ transitions. The UV-band is also present in the excitation spectrum monitored within the BDC^{2-} and $biBDC^{2-}$ ligands emission spectra (inset of Figure 9a,b), pointing out an efficient Dy^{3+} sensitization. Moreover, the higher relative intensity of the ligands broad band with respect to the Dy^{3+} lines indicates that the main excitation path for the metal ions is via the BDC^{2-} or $biBDC^{2-}$ excited states. For **Za12** the excitation spectrum monitored within the Dy^{3+} lines also reveals a broad band (390−480 nm). Figure 10 shows the emission features of the Ho^{3+}- and Er^{3+}-based materials containing $biBDC^{2-}$ ligands. The spectra reveals a broad band assigned to the ligands excited states (Supporting Information, Figure S9) and a series of Ho^{3+}- and Er^{3+}-related self-absorptions ascribed to the Er^{3+} and Ho^{3+}-related transitions, respectively. The Ho^{3+}- and Er^{3+}-doped materials containing the BDC^{2-} ligands do not show efficient room temperature emission. This observation suggests that the ligands' absorbed energy is probably being efficiently transferred to the lanthanide ions, since the ligands are optically active at 300 K

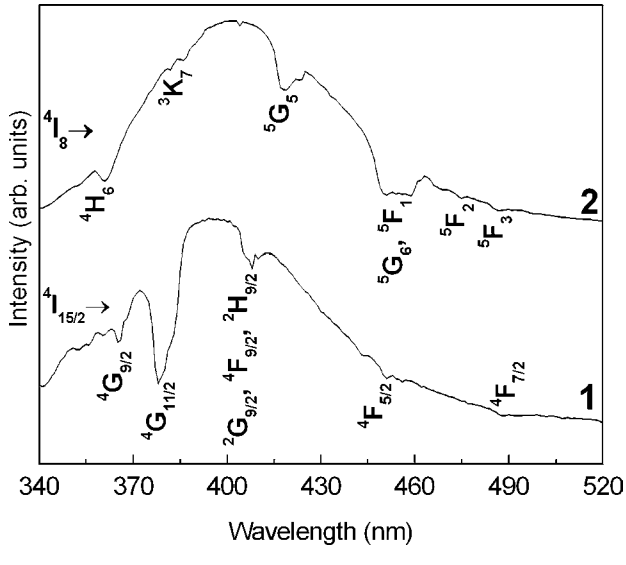

Figure 10. Emission spectra of (1) **Za16** and (2) **Za14** excited at 325 nm.

dx.doi.org/10.1021/ic202020z | *Inorg. Chem.* 2012, 51, 1703−1716

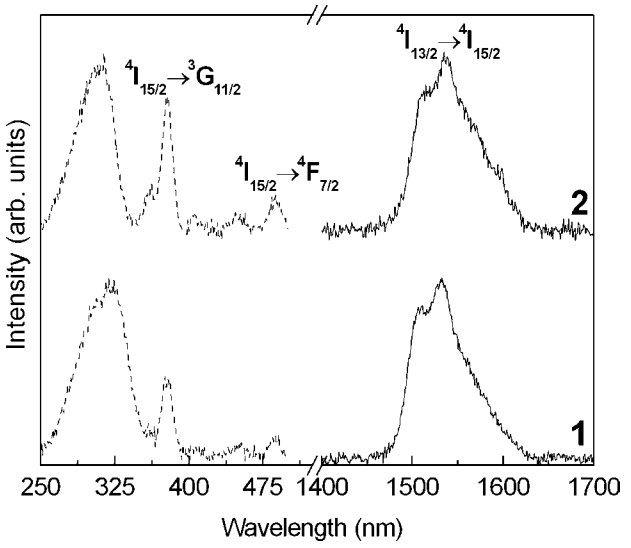

Figure 11. Excitation (dashed line) and NIR emission (solid line) spectra of (1) **Za16** and (2) **Za15** monitored around 1530 nm and excited at 325 nm, respectively.

(Supporting Information, Figure S9). Under UV excitation the Er^{3+}-containing samples display the typical NIR emission ascribed to the intra4f^{11} $^4I_{13/2} \rightarrow {}^4I_{15/2}$, Figure 11. The excitation spectra were monitored around this transition revealing a broad band ascribed to the BDC^{2-} and $biBDC^{2-}$ excited states for **Za15** and **Za16**, respectively, and a series of Er^{3+} lines attributed to the $^4I_{15/2} \rightarrow {}^3G_{11/2}$, $^4F_{7/2}$ transitions. As mentioned above for the Dy^{3+}-based materials (Figure 9), the higher-relative intensity of the ligands excited states when compared with the Er^{3+} lines points out that the lanthanide ions are mainly populated via an efficient sensitization process rather than by direct intra4f excitation.

CONCLUSIONS

In summary, the field of metal−organic frameworks chemistry has advanced quickly over recent years. Recent reports tend to focus on the functionality of these materials, but much of them are centered on transition metal rather than lanthanide containing materials because the lanthanides provide a challenge in the assembly of topologies of interest. However, it is important to harness the unique feature of the luminescent lanthanide ions and direct attention to exploring and exploiting this property for potential applications. In this context, two series $NaLn(C_4H_4O_6)(C_8H_4O_4)(H_2O)_2$ (**S1**) and $NaY(C_4H_4O_6)(C_{14}H_8O_4)(H_2O)_2$ (**S2**) made up of 16 isoreticular chiral lanthanide-organic frameworks materials based on Ln(III), Na(I), and chiral flexible-achiral rigid dicarboxylates ligands, have been synthesized and characterized. **S1** and **S2** undergo phase transformation upon dehydration process, while the spontaneous rehydration is characterized by different kinetics, fast in the case of **S1** and slow for **S2**. Catalytic activity has been quite improved through the judicious choice of the Ln^{3+} cation. Photoluminescence studies of the investigated materials show room temperature tunable UV−vis−IR light emission through an effective Ln^{3+} sensitization via BDC^{2-} and $biBDC^{2-}$ ligands.

ASSOCIATED CONTENT

Supporting Information

TG/DTG/SDTA-MS and DSC curves for the series of compounds **S1** and **S2**, emission and excitation spectra of yttrium-based compounds **Za1** and **Za2**, section of synthesis and structural characterization for **DZa7**, and X-ray crystallographic information (CIF files) for the series of compounds **S1** and **S2**, and compound **DZa7** can be obtained free of charge via the Internet at http://pubs.acs.org.

AUTHOR INFORMATION

Corresponding Author

*E-mail: amghouz.uo@uniovi.es.

ACKNOWLEDGMENTS

We thank financial support from Spanish Ministerio de Ciencia e Innovación (MAT2010-15094, MAT2006-01997, Factoría de Cristalización − Consolider Ingenio 2010, and FPI Grant BES-2007-14340 to Z.A.) and FEDER. The authors are also grateful to Prof. José Gimeno for helping us to carry out the catalysis studies.

REFERENCES

(1) (a) Kuriki, K.; Koike, Y.; Okamoto, Y. *Chem. Rev.* **2002**, *102*, 2347. (b) Polman, A.; van Veggel, F. C. J. M. *J. Opt. Soc. Am. B* **2004**, *21*, 871.
(2) (a) Justel, T.; Nikol, H.; Ronda, C. *Angew. Chem., Int. Ed.* **1998**, *37*, 3084. (b) Feldmann, C.; Justel, T.; Ronda, C. R.; Schmidt, P. J. *Adv. Funct. Mater.* **2003**, *13*, 511.
(3) (a) Yokoyama, H. *Science* **1992**, *256*, 66. (b) Adam, J. L. *Chem. Rev.* **2002**, *102*, 2461. (c) Kuck, S. *Appl. Phys. B: Laser Opt.* **2001**, *72*, 515.
(4) Dorenbos, P. *IEEE Trans. Nucl. Sci.* **2010**, *57*, 1162.
(5) (a) Hemmila, I.; Laitala, V. *J. Fluoresc.* **2005**, *15*, 529. (b) Hemmila, I.; Dakubu, S.; Mukkala, V. M.; Siitari, H.; Lovgren., T. *Anal. Biochem.* **1984**, *137*, 335. (c) Westerlund-Karlsson, A.; Suonpaa, K.; Ankelo, M.; Ilonen, J.; Knip, M.; Hinkkanen., A. E. *Clin. Chem.* **2003**, *49*, 916. (d) Ankelo, M.; Westerlund-Karlsson, A.; Ilonen, J.; Knip, M.; Savola, K.; Kankaanpaa, P.; Merio, L.; Siitari, H.; Hinkkanen, A. *Clin. Chem.* **2003**, *49*, 908. (e) Haese, A.; Vaisanen, V.; Finlay, J. A.; Pettersson, K.; Rittenhouse, H. G.; Partin, A. W.; Bruzek, D. J.; Sokoll, L. J.; Lilja, H.; Chan., D. W. *Clin. Chem.* **2003**, *49*, 601. (f) Korpimaki, T.; Hagren, V.; Brockmann, E. C.; Tuomola., M. *Anal. Chem.* **2004**, *76*, 3091.
(6) Justel, T.; Nikol, H.; Ronda, C. *Angew. Chem., Int. Ed.* **1998**, *37*, 3084.
(7) Bunzli, J. C. G.; Piguet, C. *Chem. Soc. Rev.* **2005**, *34*, 1048.
(8) (a) Chao, T. C.; Lin, Y. T.; Yang, C. Y.; Hung, T. S.; Chou, H. C.; Wu, C. C.; Wong, K. T. *Adv. Mater.* **2005**, *17*, 992. (b) Hu, X.; Deng, J.; Zhang, J. P.; Lunev, A.; Bilenko, Y.; Katona, T.; Shur, M. S.; Gaska, R.; Shatalov., M.; Khan, A. *Phys. Status Solidi A* **2006**, *203*, 1815. (c) Mochizuki, S.; Minami, S.; Fujishiro, F. *J. Lumin.* **2005**, *112*, 267.
(9) Kaye, S. S.; Dailly, A.; Yaghi, O. M.; Long, J. R. *J. Am. Chem. Soc.* **2007**, *129*, 14176.
(10) Collins, D. J.; Zhou., H. C. *J. Mater. Chem.* **2007**, *17*, 3154.
(11) Sun, D.; Ma, S.; Ke, Y.; Collins, D. J.; Zhou., H. C. *J. Am. Chem. Soc.* **2006**, *128*, 3896.
(12) Rowsell, J. L. C.; Yaghi, O. M. *J. Am. Chem. Soc.* **2006**, *128*, 1304.
(13) Ma, S.; Zhou., H. C. *J. Am. Chem. Soc.* **2006**, *128*, 11734.
(14) Wong-Foy, A. G.; Matzger, A. J.; Yaghi, O. M. *J. Am. Chem. Soc.* **2006**, *128*, 3494.
(15) Chen, B. L.; Ockwig, N. W.; Millward, A. R.; Contrereas, D. S.; Yaghi, O. M. *Angew. Chem., Int. Ed.* **2005**, *44*, 4745.
(16) Rowsell, J. L. C.; Yaghi, O. M. *Microporous Mesoporous Mater.* **2004**, *73*, 3−14.
(17) Férey, G.; Latroche, M.; Serre, C.; Millange, F.; Loiseau, T.; Percheron-Guegan, A. *Chem. Commun.* **2003**, 2976−2977.
(18) Pan, L.; Parker, B.; Huang, X.; Olson, D. H.; Lee, J. Y.; Li, J. *J. Am. Chem. Soc.* **2006**, *128*, 4180.
(19) Dinca, M.; Long, J. R. *J. Am. Chem. Soc.* **2005**, *127*, 9376.

(20) Dybtsev, D. N.; Chun, H.; Yoon, S. H.; Kim, D.; Kim., K. *Am. Chem. Soc.* **2004**, *126*, 32.
(21) Kitaura, R.; Seki, K.; Akiyama, G.; Kitagawa, S. *Angew. Chem. Intl. Ed.* **2003**, *42*, 428.
(22) Allendorf, M. D.; Bauer, C. A.; Bhakta, R. K.; Houk, R. J. T. *Chem. Soc. Rev.* **2009**, *38*, 1330.
(23) Rocha, J.; Carlos, D. C.; Almeida Paz, F. A.; Ananias, D. *Chem. Soc. Rev.* **2011**, *40*, 926.
(24) Guo, H.; Zhu, Y.; Qiu, S.; Lercher, J. A.; Zhang, H. *Adv. Mater.* **2010**, *22*, 4190.
(25) Liu, K.; You, H.; Zheng, Y.; Jia, G.; Song, Y.; Huang, Y.; Yang, M.; Jia, J.; Guo, N.; Zhang, H. *J. Mater. Chem.* **2010**, *20*, 3272.
(26) Black, C. A.; Costa, J. S.; Fu, W. T.; Massera, C.; Roubeau, O.; Teat, S. J.; Aromı, G.; Gamez, P.; Reedijk, J. *Inorg. Chem.* **2009**, *48*, 1062.
(27) Zhu, Q.; Sheng, T.; Fu, R.; Hu, S.; Chen, J.; Xiang, S.; Shen, C.; Wu, X. *Cryst. Growth Des.* **2009**, *9*, 5128.
(28) Ma, D. Y.; Liu, H. L.; Li, Y. W. *Inorg. Chem. Commun.* **2009**, *12*, 883.
(29) Li, X.; Zhang, Y. B.; Shi, M.; Li, P. Z. *Inorg. Chem. Commun.* **2008**, *11*, 869.
(30) Van der Horst, M. G.; Van Albada, G. A.; Ion, R. M.; Mutikainen, I.; Turpeinen, U.; Tanase, S.; Reedijk, J. *Eur. J. Inorg. Chem.* **2008**, 2170.
(31) Song, X. Q.; Liu, W. S.; Dou, W.; Wang, Y. W.; Zheng, J. R.; Zang, Z. P. *Eur. J. Inorg. Chem.* **2008**, 1901.
(32) Lill, D. T.; Bettencourt-Dias, A.; Cahill, C. L. *Inorg. Chem.* **2007**, *46*, 3960.
(33) Chandler, B. D.; Yu, J. O.; Cramb, D. T.; Shimizu, G. K. H. *Chem. Mater.* **2007**, *19*, 4467.
(34) Li, Z.; Zhu, G.; Guo, X.; Zhao, X.; Jin, Z.; Qiu, S. *Inorg. Chem.* **2007**, *46*, 5174.
(35) Shi, Q.; Zhang, S.; Wang, Q.; Ma, H.; Yang, G.; Sun, W. H. *J. Mol. Struct.* **2007**, *837*, 185.
(36) Mahata, P.; Natarajan, S. *Inorg. Chem.* **2007**, *46*, 1250.
(37) Sonnauer, A.; Nather, C.; Hoppe, H. A.; Senker, J.; Stock, N. *Inorg. Chem.* **2007**, *46*, 9968.
(38) Zhang, X. J.; Xing, Y. H.; Sun, Z.; Han, J.; Zhang, Y. H.; Ge, M. F.; Niu, S. Y. *Cryst. Growth Des.* **2007**, *7*, 2041.
(39) Sun, Y. Q.; Yang, G. Y. *Dalton Trans.* **2007**, 3771.
(40) Yue, Q.; Yang, J.; Li, G. H.; Li, G. D.; Chen, J. S. *Inorg. Chem.* **2006**, *45*, 4431.
(41) White, K. A.; Chengelis, D. A.; Gogick, K. A.; Stehman, J.; Rosi, N. L.; Petoud, S. *J. Am. Chem. Soc.* **2009**, *131*, 18069.
(42) Marchal, C.; Filinchuk, Y.; Chen, X.-Y.; Imbert, D.; Mazzanti, M. *Chem.—Eur. J.* **2009**, *15*, 5273.
(43) White, K. A.; Chengelis, D. A.; Zeller, M.; Geib, S. J.; Szakos, J.; Petoud, S.; Rosi, N. L. *Chem. Commun.* **2009**, 4506.
(44) Wang, H.-Y.; Cheng, J.-Y.; Ma, J.-P.; Dong, Y.-B.; Huang, R.-Q. *Inorg. Chem.* **2010**, *49*, 2416.
(45) Gandara, F.; Garcia-Cortes, A.; Cascales, C.; Gomez-Lor, B.; Gutierrez-Puebla, E.; Iglesias, M.; Monge, A.; Snejko, N. *Inorg. Chem.* **2007**, *46*, 3475.
(46) Chen, B.; Yang, Y.; Zapata, F.; Qian, G.; Luo, Y.; Zhang, J.; Lobkovsky, E. B. *Inorg. Chem.* **2006**, *45*, 8882.
(47) Herrera, J.-M.; Pope, S. J. A.; Adams, H.; Faulkner, S.; Ward, M. D. *Inorg. Chem.* **2006**, *45*, 3895.
(48) Guo, X.; Zhu, G.; Fang, Q.; Xue, M.; Tian, G.; Sun, J.; Li, X.; Qiu, S. *Inorg. Chem.* **2005**, *44*, 3850.
(49) Huang, Y. Q.; Ding, B.; Song, H. B.; Zhao, B.; Ren, P.; Cheng, P.; Wang, H. G.; Liao, D. Z.; Yan, S. P. *Chem. Commun.* **2006**, 4906.
(50) (a) Wang, M. S.; Guo, S. P.; Li, Y.; Cai, L. Z.; Zou, J. P.; Xu, G.; Zhou, W. W.; Zheng, F. K.; Guo, G. C. *J. Am. Chem. Soc.* **2009**, *131*, 13572. (b) Joao, R.; Almeida, P. F. A.; Shi, F. N.; Ferreira, R. A. S.; Tito, T.; Carlos, L. D. *Eur. J. Inorg. Chem.* **2009**, 4931.
(51) (a) Bo, Q.-B.; Sun, G.-X.; Geng, D.-L. *Inorg. Chem.* **2010**, *49*, 561. (b) Wang, H.-S.; Zhao, B.; Zhai, B.; Shi, W.; Cheng, P.; Liao, D.-Z.; Yan, S.-P. *Cryst. Growth Des.* **2007**, *7*, 1851.
(52) (a) Wang, P.; Ma, J. P.; Dong, Y. B.; Huang, R. Q. *J. Am. Chem. Soc.* **2007**, *129*, 10620. (b) Wang, P.; Ma, J. P.; Dong, Y. B. *Chem.—Eur. J* **2009**, *15*, 10432.
(53) Chen, B.; Wang, L.; Zapata, F.; Qian, G.; Lobkovsky, E. B. *J. Am. Chem. Soc.* **2008**, *130*, 6718.
(54) (a) Harbuzaru, B. V.; Corma, A.; Rey, F.; Atienzar, P.; Jordá, J. L.; García, H.; Ananias, D.; Carlos, L. D.; Rocha. *J. Angew. Chem. Int. Ed.* **2008**, *47*, 1080. (b) Chen, B.; Yang, Y.; Zapata, F.; Lin, G.; Qian, G.; Lobkovsky, E. B. *Adv. Mater.* **2007**, *19*, 1693. (c) Guo, Z.; Xu, H.; Su, S.; Cai, J.; Dang, S.; Xiang, S.; Qian, G.; Zhang, H.; O'Keeffe, M.; Chen, B. *Chem. Commun.* **2011**, *47*, 5551.
(55) Amghouz, Z.; Roces, L.; García-Granda, S.; García, J. R.; Souhail, B.; Mafra, L.; Fa-nian, S.; Rocha, J. *Inorg. Chem.* **2010**, *49*, 7917.
(56) *CrysAlis CCD*, Version 1.171.32.37 (release 24-10-2008 CrysAlis171.NET) (compiled Oct 24 2008,09:44:38), Oxford Diffraction Ltd.: Abingdon, U.K., 2008.
(57) *CrysAlis, RED*, Version 1.171.32.37 (release 24-10-2008 CrysAlis171.NET) (compiled Oct 24 2008,09:44:38); Oxford Diffraction Ltd.: Abingdon, U.K., 2008.
(58) Sheldrick, G. M. *SHELXL-97, Program for Refinement of Crystal Structures*; University of Göttingen, Germany, 1997.
(59) Burla, M. C.; Caliandro, R.; Camalli, M.; Carrozzini, B.; Cascarano, G. L.; De Caro, L.; Giacovazzo, C.; Polidori, G.; Spagna, R. *J. Appl. Crystallogr.* **2005**, *38*, 381.
(60) Parkin, S.; Moezzi, B.; Hope, H. *J. Appl. Crystallogr.* **1995**, *28*, 53.
(61) PLATON/PLUTON: (a) Spek, A. L. *Acta Crystallogr., Sect. A* **1990**, *46*, C34. (b) Spek, A. L. *PLATON, A Multipurpose Crystallographic Tool*; Utrecht University: Utrecht, The Netherlands, 1998.
(62) Brandenburg, K. *Diamond*, Version 3.1; Crystal Impact GbR, Bonn, Germany, 2007.
(63) Shannon, R. D. *Acta Crystallogr.* **1976**, *A32*, 751.
(64) Socrates, G. *Infrared and Raman CharacteristicGroup Frequencies*, 3rd ed.; Wiley: Chichester, England, 2001.
(65) Bellamy, L. J. *The Infra-red Spectra of Complex Molecules*, 3rd ed.; Chapman and Hall: London, 1975.
(66) Wang, Y. Y.; Shi, Q.; Shi, Q. Z.; Gao, Y. C.; Zhou, Z. Y. *Polyhedron* **1999**, *18*, 2009.
(67) Amghouz, Z.; Khainakov, S. A.; García, J. R.; García-Granda, S. *Z. Kristallogr. Proc.* **2011**, *1*, 361.